Resonant radiation emitted by solitary waves via cascading in quadratic media

LILI BU,[1] SHIHUA CHEN,[1,2,*] FABIO BARONIO,[3,5] AND STEFANO TRILLO[4,6]

[1] *School of Physics and Frontiers Science Center for Mobile Information Communication and Security, Southeast University, Nanjing 211189, China*
[2] *Purple Mountain Laboratories, Nanjing 211111, China*
[3] *National Inter-University Consortium for Telecommunications and Department of Information Engineering, University of Brescia, Via Branze 38, 25123 Brescia, Italy*
[4] *Department of Engineering, University of Ferrara, Via Saragat 1, 44122 Ferrara, Italy*
[5] *fabio.baronio@unibs.it*
[6] *trlsfn@unife.it*
cshua@seu.edu.cn

Abstract: We present a systematic investigation of the resonant radiation emitted by localized soliton-like wave-packets supported by second-harmonic generation in the cascading regime. We emphasize a general mechanism which allows for the resonant radiation to grow without the need for higher-order dispersion, primarily driven by the second-harmonic component, while radiation is also shed around the fundamental-frequency component through parametric down-conversion processes. The ubiquity of such a mechanism is revealed with reference to different localized waves such as bright solitons (both fundamental and second-order), Akhmediev breathers, and dark solitons. A simple phase matching condition is put forward to account for the frequencies radiated around such solitons, which agrees well with numerical simulations performed against changes of material parameters (say, phase mismatch, dispersion ratio). The results provide explicit understanding of the mechanism of soliton radiation in quadratic nonlinear media.

1. Introduction

Optical resonant radiation (RR), also referred to as Cherenkov radiation [1], was first observed in numerical simulations performed in the vicinity of zero-dispersion wavelength of optical fibers [2]. Shortly afterward, its experimental observation was reported in the context of single-mode optical fibers [3], demonstrating that fiber solitons, supported by the interplay between anomalous group-velocity dispersion (GVD) and focusing Kerr nonlinearity, can resonantly transfer energy towards linear dispersive waves with shifted frequency. It turns out that a crucial ingredient for such an energy transfer is the presence of higher-order dispersion which allows for the resonant phase matching between the soliton and the radiated linear waves, thus constituting a remarkable example of the RR effects of dispersive perturbations of solitons [4,5]. Nowadays, the mechanisms of primary RR in cubic Kerr-like media and its interaction with solitons are pretty well understood, and form the basis of many applications that exploit the properties of tunability via dispersion tailoring and/or RR-induced spectral broadening devoted to spectroscopy [6–8], supercontinuum generation [9–14], and spectral shaping of frequency combs in microresonators [15–17] or four-wave mixing combs in fibers [18,19], as well as the generation of far detuned spectral lines [20], to name a few.

On the other hand, it is also well known that quadratic nonlinearities support solitary wave formation, with second-harmonic generation (SHG) being the most common example demonstrating solitons (see review in [21]). Indeed, extensive research has been conducted on pulse compression and localization in quadratic media in the form of two-color soliton-like pulses

[22–26]. In the cascading (i.e., large absolute mismatch) regime, pulses can be trapped in either the anomalous or normal GVD regime by adjusting the sign of nonlinearity. The fact that the emission of RR can be driven by quadratic solitons has been theoretically predicted [27–29], and experimentally demonstrated in bulk BBO crystals [30–32] or in periodically poled lithium niobate [33], by injecting pulses in the normal GVD regime for a defocusing effective nonlinearity. To date, the proposed interpretation of such results relies on considering the new generated RR frequencies as being produced through the phase-matching favoured by higher-order dispersion (eventually at all-order ones), in close analogy to the case of cubic nonlinearity.

However, RR emitted through cascaded SHG does not necessarily need the effective contribution from higher-order dispersion. Indeed, as we have recently shown in [34] for the example of a quadratic Peregrine soliton (PS), RR can be emitted efficiently also when GVD remains the dominant term, i.e., not in the vicinity of a zero GVD wavelength. This feature is not expected to stem from the specific properties of the PS (indeed, in cubic media, PSs are found to radiate only when higher-order dispersion is effective [35]), but rather from the intrinsic characteristic of the multi-component quadratic cascaded interaction. In fact, under appropriate conditions, the weaker second-harmonic (SH) component of the soliton can resonate with linear waves producing primary new RR frequency lines, which in turn lead to RR around the fundamental frequency (FF) via frequency conversion (FC, specifically down-conversion) processes [34].

The aim of this article is to show that this mechanism is rather universal, occurring, in the cascading regime, for a wide class of quadratic solitary waves sustained by $\chi^{(2)} : \chi^{(2)}$ cascading. To this end, we consider both wavepackets with zero background, namely fundamental solitons and higher-order solitons normally exploited to achieve temporal compression, as well as the Akhmediev breathers (ABs) [36–39] and dark solitons with non-zero background. In particular, ABs are important in the framework of modulation instability, being able to describe the growth and decay cycle of unstable modulation frequencies, with the PS representing the limit of such behavior for vanishing modulation frequency. Our goal is to show that all of such solitons radiate even without any contribution from higher-order dispersion. As we will show, the resulting RR frequencies are predictable with good accuracy in terms of simple phase-matching formulas, which we validate by performing extensive numerical simulations for a wide range of relevant parameters, mainly the ones defining the phase mismatch and GVD ratio.

The subsequent sections are organized as follows. In Sec. 2, we recall the pertinent models for SHG and their cascading limit, along with the phase-matching argument. The specific cases of the RR emitted by fundamental and second-order solitons are discussed in Secs. 3 and 4, respectively. Section 5 is devoted to the discussion of the radiating AB. In Sec. 6, we briefly mention the case of radiating dark solitons. Finally, our findings are summarized in Sec. 7.

2. Theoretical model and radiative phase matching

Pulse propagation describing the interaction between the FF and the SH pulses in quadratic dispersive media is governed by the following two dimensionless coupled equations [21]:

$$iu_{1\xi} - \frac{\beta_1}{2}u_{1\tau\tau} + u_2 u_1^* e^{-i\delta k\xi} = 0,$$
$$iu_{2\xi} + iv u_{2\tau} - \frac{\beta_2}{2}u_{2\tau\tau} + u_1^2 e^{i\delta k\xi} = 0, \tag{1}$$

where $u_{1,2}(\xi, \tau) = \chi z_d A_{1,2}$ are the normalized envelopes of the FF and the generated SH components in a reference frame comoving with the FF group velocity v_1. The subscripts ξ and τ stand for the derivatives with respect to propagation distance $\xi = z/z_d$ in units of the dispersion length $z_d = t_0^2/\beta_1''$ and the delayed time $\tau = (t - z/v_1)/t_0$ in units of input pulse duration t_0. The parameter $\beta_1 = \beta_1''/|\beta_1''| = \pm 1$ stands for the GVD sign at FF, and $\beta_2 = \beta_2''/\beta_1''$ is the dispersion ratio of the SH GVD $\beta_2'' = d^2k/d\omega^2|_{2\omega_0}$ to the FF one $\beta_1'' = d^2k/d\omega^2|_{\omega_0}$, for specific propagation

constant $k(\omega)$. v is the group-velocity mismatch of the SH wave measured in the FF group velocity frame, and $\delta k = \Delta k z_d = (2k_1 - k_2)z_d$ is the normalized wavenumber (or phase) mismatch, where $k_{1,2} = k|_{\omega_0, 2\omega_0}$. Here $\chi = \omega_0 d^{(2)}(c^3 \epsilon_0 n_{\omega_0}^2 n_{2\omega_0})^{1/2}$, ϵ_0 is the permittivity of free space, c is the light speed in vacuum, $n_{\omega_0, 2\omega_0}$ are refractive indexes of quadratic medium evaluated at FF and SH, $d^{(2)}$ is the effective nonlinear element (m/V), and $|A_{1,2}|^2$ measures the intensity of FF and SH waves (W/m^2). We emphasize that Eqs. (1) can also describe the propagation of spatial beams confined in one transverse dimension, with τ being the normalized transverse spatial coordinate and v the birefringent walk-off [21].

Considering the strong phase-mismatched SHG (i.e., in the cascading limit $|\delta k| \gg 1$), the $\chi^{(2)}$ nonlinearity of FF in Eqs. (1) can be approximately described by an effective $\chi^{(3)}$ nonlinearity, which can be obtained by using the SH asymptotic expansion $u_2 = \sum_{n=0}^{\infty} u_2^{(n)}/\delta k^n$ and the method of repeated substitution. What is relevant here is the integrable nonlinear Schrödinger (NLS) equation, which can be easily obtained at first-order approximation [21,40,41],

$$i\rho_\xi - \frac{\beta_1}{2}\rho_{\tau\tau} + \kappa|\rho|^2\rho = 0, \tag{2}$$

where $\kappa = 1/\delta k$ is the effective Kerr nonlinear coefficient, and the envelope $\rho(\xi, \tau)$ allows to calculate the fields (at first order in the expansion) as

$$u_1(\xi, \tau) = \rho(\xi, \tau), \quad u_2(\xi, \tau) = \frac{\rho^2(\xi, \tau)}{\delta k}e^{i\delta k\xi}. \tag{3}$$

In cascaded SHG, the existence of nonlinear localized waves ruled by Eq. (2), or by the Chen-Lee-Liu equation obtained at second order [42–44], has been demonstrated, either numerically or experimentally, which includes but not limited to shape-invariant and compressing solitons, shock waves, ABs, and PSs [21–26,37–45]. Generally speaking, such localized waves are sustained by the interplay between GVD and Kerr-like nonlinearities, due to the repeated conversion and back-conversion occurring at large mismatch. However, the mechanisms of resonance with linear waves can make these nonlinear waves radiate spontaneously. In the following sections, we deepen the analysis of such mechanism by looking into the relevant cases of the fundamental bright soliton, the second-order bright soliton, the AB, as well as the dark soliton.

Dispersive waves are linear waves that can form in any dispersive medium under different mechanisms (e.g., using an input that presents a small deviation from a nonlinear localized wave). Generally, for their amplitude remains small, such dispersive waves are apt to be dispersed away upon propagation. Conversely, when they turn out to be phase-matched to a nonlinear localized wave that acts as a pump, they can resonantly grow and then stabilize. In nonlinear optics, the RR can be considered as being phase-matched along the propagating direction ξ. We start by assuming a generic nonlinear pump wave of FF and SH components, respectively:

$$u_{jnl}(\xi, \tau) = \rho_j(\xi, \tau)\exp(ik_{jnl}\xi), \quad j = 1, 2, \tag{4}$$

where $k_{1nl}(k_{2nl})$ is the nonlinear wavenumber shift of the FF (SH) wave component at carrier pulsation ω_0 ($2\omega_0$), and $\rho_{1,2}(\xi, \tau)$ are ξ-dependent envelopes that can account for the internal dynamics of the unperturbed nonlinear (solitary) waves. We consider their resonance with linear dispersive waves defined by

$$u_{jlin}(\xi, \tau) = \exp(ik_{jlin}\xi - i\omega_j\tau_p), \quad j = 1, 2, \tag{5}$$

where $k_{1lin}(k_{2lin})$ is the linear wavenumber of the dispersive wave emitted around FF (SH), and $\tau_p = \tau - v_p\xi$ is a retarded time in the framework traveling with the walking velocity v_p of the nonlinear wave. In this framework, linear dispersive waves can extract energy at the expense of

the nonlinear wave when the following phase-matching relations are fulfilled:

$$k_{1\text{lin}} = k_{1\text{nl}}, \quad k_{2\text{lin}} = k_{2\text{nl}}. \tag{6}$$

By substituting the linear waves into Eqs. (1) and dropping nonlinear terms, we obtain the explicit dependence of the wavenumbers $k_{j\text{lin}}, j = 1, 2$ on frequency detunings ω_j, which when inserted back into Eqs. (6) yield the explicit phase-matching relations:

$$\frac{1}{2}\beta_1\omega_1^2 - v_p\omega_1 = k_{1\text{nl}}, \tag{7a}$$

$$\frac{1}{2}\beta_2\omega_2^2 - (v_p - v)\omega_2 = k_{2\text{nl}}. \tag{7b}$$

Solutions $\omega_1 = \omega_{1RR}$ and $\omega_2 = \omega_{2RR}$ of Eqs. (7) give the possible normalized detunings of the phase-matched RR around FF and SH, respectively. In the next sections, we exploit Eqs. (7) to predict the RR emitted by different types of soliton-like nonlinear waves. For sake of simplicity, here we restrict our consideration to the case of group-velocity matching ($v = 0$) and stationary solitary waves ($v_p = 0$), although as explicitly shown in [34], the present consideration can be extended to the regime of walk-off where the solitons will be of the walking type.

3. Fundamental bright solitons

In cascaded SHG, bright solitons ruled by Eq. (2) are allowed to exist in either the normal ($\beta_1 = 1$) or the anomalous ($\beta_1 = -1$) GVD regime at FF, under the soliton constraint $\beta_1 \delta k < 0$. Here we are concerned with the latter case ($\beta_1 = -1$, $\delta k > 0$; the extension to the former case is straightforward), and analyse the RR mechanism for the fundamental soliton solution of Eq. (2), which reads, without loss of generality, as

$$\rho_{\text{sol}}(\xi, \tau) = \sqrt{2}\text{sech}(\alpha\tau)\exp(i\kappa\xi), \tag{8}$$

where we take $\kappa \equiv 1/\delta k$ and $\alpha \equiv \sqrt{2\kappa}$.

We recall the well-known fact that the temporal envelope of such soliton has constant modulus and flat phase, whereas, with distance, the amplitude is constant and only the phase accumulates linearly due to a constant nonlinear wavenumber $k_{1\text{nl}} = \kappa \equiv 1/\delta k$. In order to easily compare with the more complicated cases of the following sections, we illustrate these features in Fig. 1.
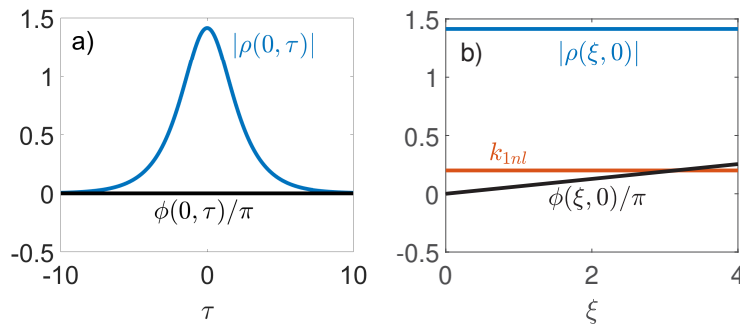

Fig. 1. Fundamental soliton: (a) envelope amplitude $|\rho_{\text{sol}}(0, \tau)|$ (solid blue) and phase $\phi(0, \tau)/\pi$ (solid black) temporal profiles; (b) spatial longitudinal profile of phase $\phi(\xi, 0)/\pi$ (solid black), peak amplitude $|\rho_{\text{sol}}(\xi, 0)|$ (solid blue), and wavenumber $k_{1\text{nl}}$ (solid orange). Here $\beta_1 = -1$, $\delta k = 5$.

The RR from the components at FF and SH of the fundamental soliton can be well anticipated for linear waves with frequency detuning given by real solutions $\omega_j = \omega_{jRR}, j = 1, 2$ of Eqs. (7), which, in this case, are cast in explicit form as

$$\frac{\beta_1}{2}\omega_{1RR}^2 = \kappa, \tag{9a}$$

$$\frac{\beta_2}{2}\omega_{2RR}^2 = \delta k + 2\kappa, \tag{9b}$$

where the terms on the right-hand side stand for the wavenumber of the solitary waves allowed, as is evident from Eqs. (3). Owing to the essential constraint for the soliton existence $\beta_1 \kappa < 0$, Eq. (9a) has no real solutions which expresses the well-known fact that solitons cannot be in resonance with linear waves unless higher-order dispersion plays a relevant role, i.e. when operating around a vanishing GVD wavelength. However, a resonance can still occur through the weaker SH component of the soliton. Indeed Eq. (9b) can have solutions $\omega_{2RR}^{\pm} = \pm\sqrt{(2\delta k + 4\kappa)/\beta_2}$, provided that the GVD at SH has opposite sign of GVD at FF, i.e., $\beta_1\beta_2 < 0$.

We have numerically verified the emission of this type of RR by integrating numerically the SHG model Eqs. (1) using a pseudo-spectral method (known also as split-step Fourier technique), and initial values $u_1(0, \tau) = \rho_{\text{sol}}(0, \tau)$ and $u_2(0, \tau) = \rho_{\text{sol}}^2(0, \tau)/\delta k$ according to Eqs. (3). A typical example is shown in Fig. 2 for $\delta k = 5$ and equal moduli of GVD at FF and SH (i.e., $\beta_2 = 1$). As shown in Fig. 2(a), the FF component propagates nearly unperturbed with most of the energy confined in the localized pulse, whereas the SH component undergoes, since the early stage of propagation, weak breathing (temporal compression and oscillation of the peak) while symmetrically emitting RR from both the leading and the trailing edges [see Fig. 2(b)]. The spectral evolutions of FF and SH waves in logarithmic scale are presented in Figs. 2(c) and 2(d) with the spectral output profiles at $\xi = 10$ displayed in the upper panels. The new radiated frequencies are produced around $\omega_{2RR}^{\pm} = \pm 3.28$, which are fully consistent with the prediction from Eq. (9b), reported as dashed lines in Figs. 2(c) and 2(d) and marked by bullets in the output spectral cuts. We also illustrate in Fig. 3 the evolutions of the generated SH component, filtered around $\omega_{2RR}^{\pm}$. It is seen that the RR shed from the SH component fills a temporal fan which is delimited by the soliton (zero velocity) and a maximal velocity that can be estimated from the linear approximation $v_{RR}^{\pm} \approx \beta_2\omega_{2RR}^{\pm}$ (dashed oblique lines in Fig. 3).

Despite the absence of direct phase matching of the FF component, RR can also grow around FF through non-degenerate FC processes of the down-conversion type, which can be conveniently expressed by returning to real-world detunings $\Delta_{1,2} = t_0^{-1}\omega_{1,2}$. Indeed, the RR detuned (from SH) by $\Delta_2 = \Delta_{2RR}^{\pm}$ corresponds to photons at physical pulsations $2\omega_0 + \Delta_{2RR}^{\pm}$, which undergo a three-photon difference FC process $2\omega_0 + \Delta_{2RR}^{\pm} - \omega_0 = \omega_0 + \Delta_{1FC}^{\pm}$. The conservation of energy implies equal detunings from FF and SH, i.e., $\Delta_{1FC}^{\pm} = \Delta_{2RR}^{\pm}$. In terms of normalized units, this means to have sidebands around the FF at $\omega_{1FC}^{\pm} = \omega_{2RR}^{\pm} = \pm 3.28$, which are highlighted by the dashed lines in Figs. 2(c) and relative bullets in the output spectral profiles. The intensity of the RR around the FF, however, is such that it can be hardly seen in the temporal domain.

We have conducted extensive simulations to assess the dependence of the RR excitation on the mismatch parameter δk and the GVD ratio parameter β_2 that affect SHG. We compare in Fig. 4(a) the predicted RR frequency (solid curves) with the data extracted from the simulation (dots) versus δk at different values of the normal GVD of the SH component. The RR frequencies are reported in a range of mismatch δk sufficiently small for the RR to be detectable. Indeed the RR becomes too far detuned from the central frequency to be detected when the mismatch becomes too large. For instance, for $\beta_2 = 0.5$, the range of $\delta k \geq 15$ does not lead to significant RR, while for the larger GVD ratio, e.g., $\beta_2 = 5$, the RR frequency can be excited even at larger mismatch, as a result of being closer to the pump frequency. Our predictions agree well with the numerical simulations in the full range. In Fig. 4(b) we illustrate the dependence of the RR efficiency on δk
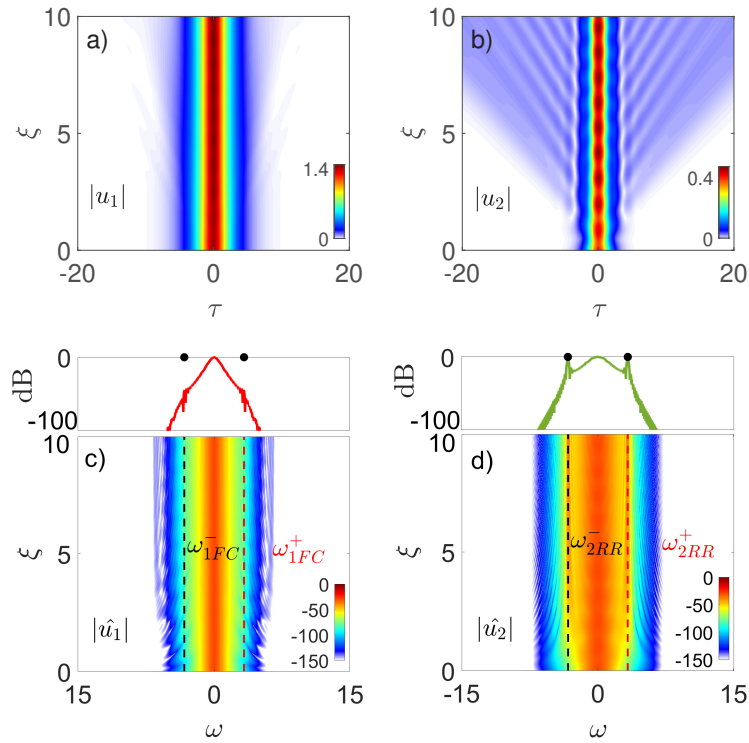
Fig. 2. Fundamental soliton: numerical spatiotemporal dynamics of the (a) FF and (b) SH components and their corresponding spectra (c) and (d). In (c) and (d) the dashed lines labelled by $\omega_{2RR}^{\pm} = \omega_{1FC}^{\pm} = \pm 3.28$ stand for the RR frequencies from Eq. (9b) and the top cuts display the output ($\xi = 10$) spectral profiles of FF and SH waves, with bullets indicating the predicted frequencies. Here $\beta_1 = -1$, $\beta_2 = 1$, and $\delta k = 5$.
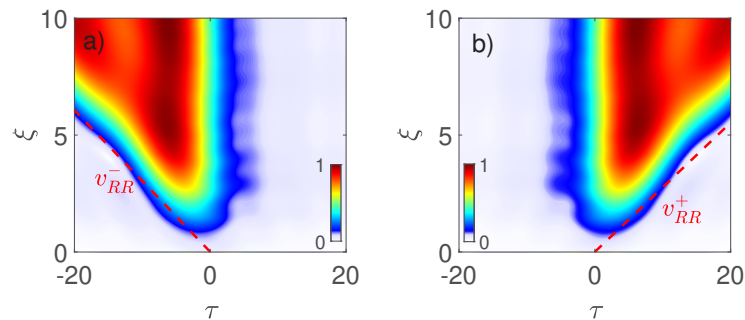

Fig. 3. Normalized spatiotemporal SH dynamics (case of Fig. 2(b)), after filtering around resonant frequencies (a) $\omega_{2RR}^{-} = -3.28$ and (b) $\omega_{2RR}^{+} = 3.28$.

and β_2 at SH, defined as the ratio (in log units) of spectral intensities between the output RR and the input pump, i.e., $10\log_{10}|\tilde{u}_2(\omega_{2RR}^{\pm},\xi)|^2/|\tilde{u}_2(0,0)|^2$, where $\tilde{u}_2$ denotes the Fourier transform of u_2. We display such efficiency at $\xi = 10$ where it saturates, no longer showing relevant growth for longer distances. Essentially, as shown, such efficiency drops for large mismatches because the cascading nonlinearity becomes weaker (its strength scales like $1/\delta k$), as well as for smaller GVD ratios β_2, because the RR frequencies increase (which scale with $|\beta_2|^{-1/2}$) and hence become less efficiently seeded due to the exponential decay of the soliton spectral tails.
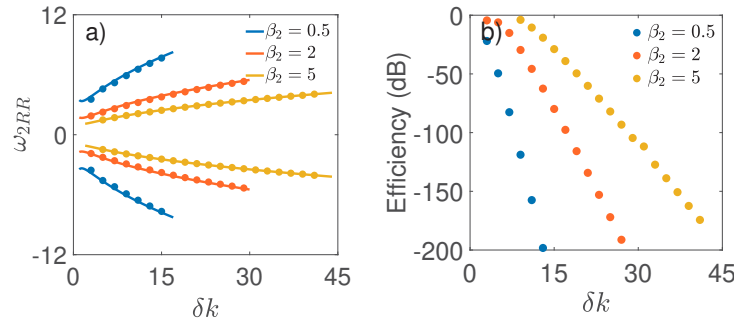

Fig. 4. (a) Theoretical results from Eq. (9b) (solid lines) and numerical simulations (dots) of RR frequencies ω_{2RR} versus the mismatch δk, for different β_2. (b) RR efficiency at ω_{2RR} calculated numerically at $\xi = 10$ versus δk. Here $\beta_1 = -1$.

4. Second-order bright solitons

The second-order soliton solution of Eq. (2), known also as the $N = 2$ breather with zero background, can be expressed in our units as [46]

$$\rho_{\mathrm{sol}}(\xi,\tau) = \frac{4\sqrt{2}[\cosh(3\alpha\tau) + 3e^{8i\kappa\xi}\cosh(\alpha\tau)]}{\cosh(4\alpha\tau) + 4\cosh(2\alpha\tau) + 3\cos(8\kappa\xi)}e^{i\kappa\xi}, \tag{10}$$

whose initial form at $\xi = 0$ is given by

$$\rho_{\mathrm{sol}}(0,\tau) = 2\sqrt{2}\mathrm{sech}(\alpha\tau), \tag{11}$$

i.e., simply twice the initial input of fundamental soliton. According to Eqs. (3), the corresponding quadratic FF and SH waves are $u_1(\xi,\tau) = \rho_{\mathrm{sol}}(\xi,\tau)$, $u_2(\xi,\tau) = \rho_{\mathrm{sol}}(\xi,\tau)^2\exp(i\delta k\xi)/\delta k$.

The second-order soliton defined by Eq. (10) possesses the characteristic longitudinally periodic structure common to the Nth-order soliton breathers, which oscillates along the propagation direction with spatial period $\pi/4\kappa$ (in our units). The peak amplitude $4\sqrt{2}$ is reached at $\xi_m = (2m + 1)\pi/8\kappa$, with m being an integer number. This dynamics can be well appreciated within Fig. 5, which reports the first two cycles of the periodic evolution according to the analytical solution (10), for $\kappa = 1/24$. In particular, Figs. 5(a) and 5(b) show the typical cycles of temporal compression and corresponding spectral broadening, respectively. At the point of maximal compression (or maximal spectral broadening), the temporal profile shows a peak and two neighbouring zeros, across which the phase shows a jump of π, as shown in Fig. 5(c). We remark that this feature is similar to a PS, though, in the present case, the solution vanishes instead of returning to a finite background at $\tau = \pm\infty$.

A major important difference with the fundamental soliton is that, in this case, besides the constant nonlinear phase shift $\kappa\xi$, the soliton exhibits a local (in ξ) contribution to the nonlinear phase, say $\phi_{\mathrm{loc}}(\xi,0)$, which arises from the ξ-dependent complex envelope [see fraction in
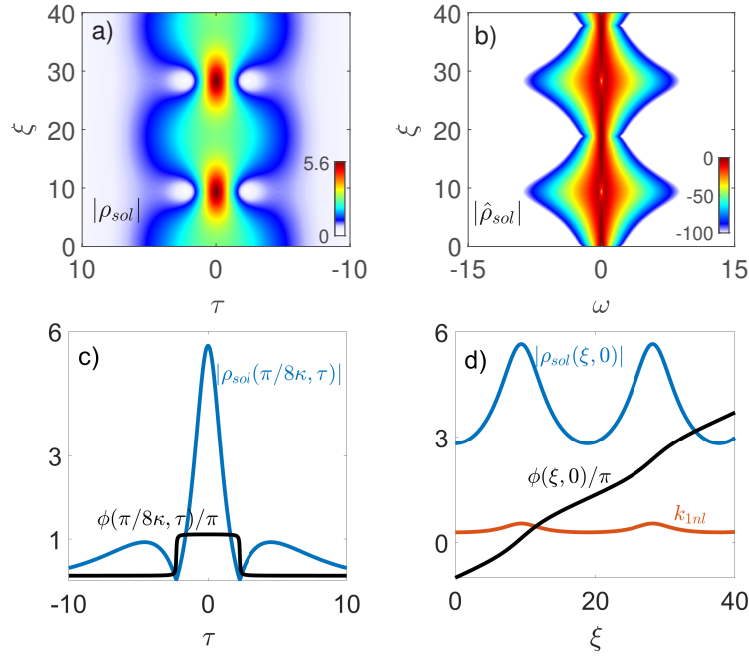
Fig. 5. Second-order soliton: (a) dynamics of the analytical spatiotemporal envelope of Eq. (10) and (b) the corresponding spectrum; (c) temporal amplitude profile $|\rho_{sol}(\pi/8\kappa, \tau)|$ (solid blue) and phase $\phi(\pi/8\kappa, \tau)/\pi$ (solid black) at the point of maximum compression $\xi = \pi/8\kappa$; (d) longitudinal phase profile $\phi(\xi, 0)/\pi$ (solid black), peak amplitude $|\rho_{sol}(\xi, 0)|$ (solid blue), and overall nonlinear wavenumber k_{1nl} (solid orange). Here $\delta k = 24$, $\beta_1 = -1$.

Eq. (10)]. The spatial evolution of such phase $\phi_{loc}(\xi, 0)$, which reads explicitly as

$$\phi_{loc}(\xi, 0) = \tan^{-1}\left[\frac{3\sin(8\kappa\xi)}{1 + 3\cos(8\kappa\xi)}\right], \tag{12}$$

is displayed in Fig. 5(d). The spatial derivative of such phase represents a local contribution, say k_{loc}, to the overall nonlinear wavenumber of the soliton [35]:

$$k_{loc} = \left.\frac{\partial\phi_{loc}}{\partial\xi}\right|_{(\xi,0)} = \frac{12\kappa(3 + \cos(8\kappa\xi))}{5 + 3\cos(8\kappa\xi)}, \tag{13}$$

which, as shown in Fig. 5(d), peaks at the maximum compression points.

As a result, when dealing with a stationary second-order soliton, the phase-matching conditions must be generalized to account for such a local contribution to the nonlinear shift, yielding

$$\frac{\beta_1}{2}\omega_{1RR}^2 = \kappa + k_{loc}, \tag{14a}$$

$$\frac{\beta_2}{2}\omega_{2RR}^2 = \delta k + 2\kappa + 2k_{loc}. \tag{14b}$$

Only the second of these equations, Eq. (14b), has real solutions and therefore predicts the occurrence of equally up- and down-shifted RR with detuning $\omega_{2RR}^{\pm} = \pm\sqrt{(2\delta k + 4\kappa + 4k_{loc})/\beta_2}$. As pointed out above, no real solutions can arise from Eq. (14a).

In order to illustrate the impact of the full SHG dynamics on the second-order soliton, we have simulated the pulse propagation by the initial condition $u_1(0, \tau) = \rho_{sol}(0, \tau)$, $u_2(0, \tau) =$

$\rho_{\text{sol}}^2(0, \tau)/\delta k$ in the full SHG model. The typical evolutions of FF and SH waves are displayed in Fig. 6 for $\delta k = 24$, $\beta_1 = -1$, $\beta_2 = 1$, exhibiting significant RR from the SH pump component at each maximum compression point [see Fig. 6(b)]. It is shown that RR of opposite detunings travel away from the SH pump pulse in opposite directions, with estimated RR velocity $v_{RR}^{\pm} = \beta_2 \omega_{2RR}^{\pm}$. Conversely, no direct RR is visible in the temporal evolution of the FF component in Fig. 6(a). Figures 6(c) and 6(d) illustrate the corresponding spectral evolutions in the (ω, ξ) plane. The spectrum in Fig. 6(d) confirms the generation of symmetric RR lines with detuning $\omega_{2RR}^{\pm} = \pm 7.08$ from the SH. It is clear that the initial emission of dispersive radiation occurs primarily when the soliton spectrum broadens considerably to overlap with the resonant frequency. Remarkably, the spectrum in Fig. 6(c) suggests that (weaker) RR around the FF with detuning $\omega_{1FC}^{\pm} = \omega_{2RR}^{\pm}$ may take place as well, despite the absence of direct phase-matching in Eq. (14a). This is ascribed to the down-conversion process already discussed in Sec. 3 for the fundamental soliton. Note also that Fig. 6(d) shows an additional, much weaker, pair of RR sidebands, which, however, cannot be explained in terms of the simple phase-matching argument given in this paper.
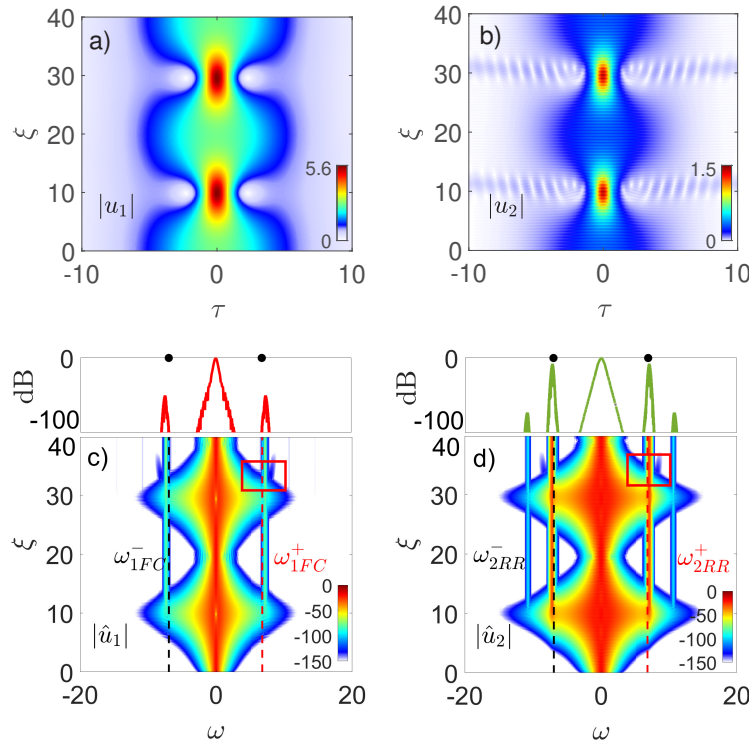

Fig. 6. Numerical spatiotemporal envelope dynamics of the (a) FF and (b) SH components and their corresponding spectra (c) and (d); in (c),(d) the dashed lines labelled by $\omega_{2RR}^{\pm}$, $\omega_{1FC}^{\pm}$ stand for the RR frequencies predicted via Eq. (14b), the top cuts display the output spectral profiles of FF and SH waves at $\xi = 40$, with bullets indicating the predicted frequencies. The red box around $\xi \simeq 35$ identifies the portion of the spectrum zoomed in the inset of Figs. 7(a),(b). Here $\delta k = 24$, $\beta_1 = -1$, $\beta_2 = 1$.

Noteworthily, when zooming in on the spectra around ω_{2RR}^{+} and ω_{1FC}^{+} (or around symmetric negative frequencies), at sufficiently large distances [i.e., $\xi \approx 35$, see red box in Figs. 6(c) and 6(d)], the RR appears to cover an extended bandwidth within which the RR possesses a fine comb-like structure, as shown in Figs. 7(a) and 7(b). This can be understood by considering that, in the presence of any longitudinal periodicity, the phase-matching becomes affected by

quasi-momentum terms $q2\pi/\Lambda$, where Λ is the characteristic period and $q = 0, \pm1, \pm2, \ldots \in \mathbb{Z}$ (i.e., harmonic order associated with the periodicity). This concept holds true regardless of the fact that the periodicity is built-in in the structure (e.g., quasi-phase-matching [47], dispersion oscillating fibers [48]; we refer the readers to the detailed calculation in [49]) or intrinsic to the nonlinear evolution of the pump wave [50], as in the present case. By taking into account the quasi-momentum contribution associated with soliton period $\Lambda = \pi/4\kappa$, Eq. (14b) can be transformed into

$$\frac{\beta_2}{2}\omega_{2RR}^2 = \delta k + 2\kappa + 2k_{\text{loc}} + q8\kappa, \quad q = 0, \pm1, \pm2, \ldots. \tag{15}$$

Such relation could predict with good accuracy the polychromatic comb structures of the RR shown in Figs. 7(a) and 7(b), which are obtained from the spectra centering around ω_{1FC}^+ and ω_{2RR}^+ in Figs. 6(c) and 6(d) at $\xi = 40$, respectively. Indeed, in Fig. 7 the colored vertical lines, which correspond to different q values in Eq. (15), give a good approximation of the observed peaks of the comb structure obtained numerically, despite that the latter are obtained after only two soliton periods. In particular, the above formula gives a sufficiently precise estimate of the average (as the spectral peaks are not strictly equi-spaced) spacing $\Delta\omega_{2RR} = 0.47$ observed from the numerics at both FF and SH. We note that such fine structure can be reminiscent of that observed in Kerr media [50]. However, while the latter shows up in the regime of sufficiently small but finite third-order dispersion, in the current quadratic case, no such dispersion is needed, thanks to the contribution of the GVD at SH. We also remark that the same filtering applied to all distances ξ, as shown in Fig. 8, allows us to observe the fact that the RR tends to separate from the soliton with its own velocity $v_{RR}^\pm \approx \beta_2\omega_{2RR}^\pm$ (see black dashed line in Fig. 8).
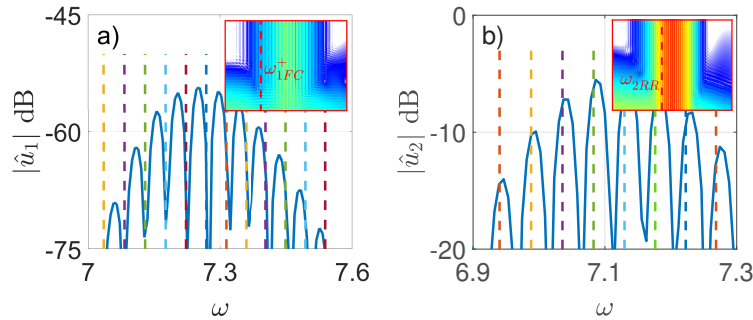

Fig. 7. Output (a) FF and (b) SH spectral profiles at $\xi = 40$. The insets show the zoomed FF and SH spectra in the red boxes in Fig. 6 centered around $\xi = 35$ and $\omega_{1FC}^+ = 7.08$ and $\omega_{2RR}^+ = 7.08$, respectively. The colored vertical lines represent the theoretical RR frequencies evaluated from Eq. (15) with variable integer q.

Finally, we conclude this section by plotting the dependence of the RR central frequency (of the comb structure) on the mismatch δk, for different values of the GVD ratio β_2 (see Fig. 9). It is exhibited that the theoretical predictions of Eq. (14b) (solid lines) agree well with the numerical simulations (dots). We point out that the k_{loc} term in Eq. (14b) turns out to be nearly negligible in all cases, except for small values of the mismatch δk.
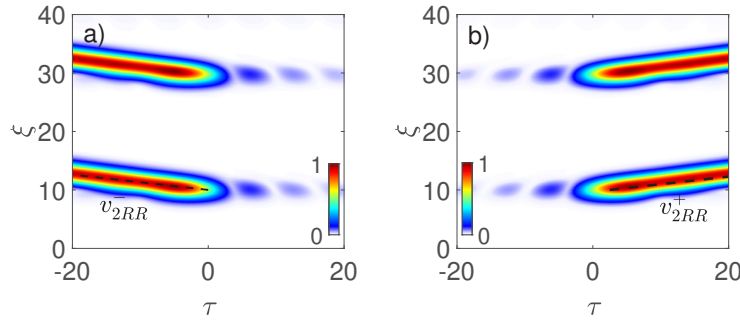
Fig. 8. Numerical normalized SH component extracted from Fig. 6, filtered around RR frequencies (a) $\omega_{2RR}^- = -7.08$ and (b) $\omega_{2RR}^+ = 7.08$, respectively.
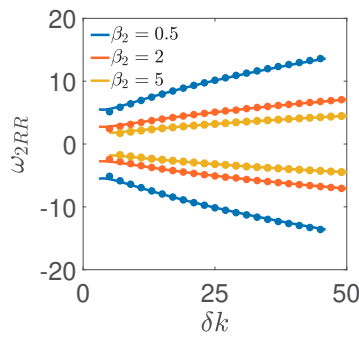

Fig. 9. RR frequencies $\omega_{2RR} = \omega_{2RR}^\pm$ versus mismatch δk for different β_2. The solid lines and dots indicate the theoretical predictions from Eq. (14b) and the numerical simulations, respectively. Here $\beta_1 = -1$.

5. Akhmediev breathers

The aim of the current section is to show that the mechanism of dispersive wave generation discussed so far for coherent excitations with smooth temporal profiles (solitons with zero background in the previous sections and Peregrine breathers on finite background in [34]) is valid also for time-periodic breathers known as ABs [36–38]. The importance of ABs relies on the fact that they generalize the Peregrine breathers, and in practical experiments on modulation instability with finite modulation frequency, they discriminate qualitatively different recurrent evolutions in the nonlinear stage of modulation instability [39,48]. We start from the AB solution of Eq. (2) that is valid under the condition $\beta_1 \delta k < 0$ [36,51],

$$\rho_{\text{AB}}(\xi, \tau) = \rho_0 \left[\frac{(1 - 4a)\cosh(\xi_n) + \sqrt{2a}\cos(\tau_n) + ib\sinh(\xi_n)}{\sqrt{2a}\cos(\tau_n) - \cosh(\xi_n)} \right], \tag{16}$$

where $\rho_0 = e^{i\kappa\xi}$, and $\xi_n = b\kappa\xi$ and $\tau_n = \Omega\sqrt{\kappa}\tau$ are suitable renormalization of space and time which depend on the nonlinear coefficient κ in Eq. (2), with Ω being the modulation frequency.

The ABs are parameterized by the parameter $a = (1 - \Omega^2/4)/2$, $0 \le a \le 1/2$, which fixes the modulation frequency Ω in the unstable region and the corresponding growth rate (gain) given by $b = \sqrt{8a(1 - 2a)}$. The corresponding FF u_1 and SH u_2 envelopes of the quadratic ABs are obtained from Eqs. (3), with $\rho(\xi, \tau) = \rho_{\text{AB}}(\xi, \tau)$ from Eq. (16). In the following we show representative examples obtained for $\Omega = 0.3$ ($a = 0.488, b = 0.296$), though similar results are obtained in the range of unstable frequencies $0 \le \Omega \le 2$. Figure 10 displays the typical

evolution of an AB according to Eq. (16), for $\beta_1 = -1$ and $\delta k = 5$. As shown in Fig. 10(a), the AB exhibits a single cycle of growth and decay of peaks separated in time by $2\pi/\Omega$ over the unit background. At the apex ($\xi = 0$) where the amplitude reach nearly three times the background and the field exhibits characteristic phase jumps of π [see Fig. 10(c)], the AB shows its maximum spectral broadening [see Fig. 10(b)], which serves as a seeding mechanism in the presence of phase-matching for the RR frequencies.
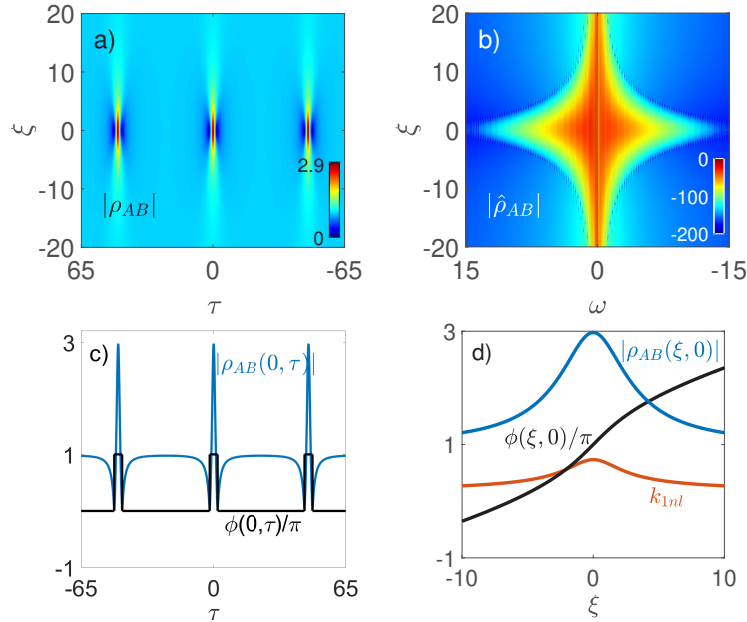

Fig. 10. (a) Spatiotemporal evolution of the AB; (b) the corresponding spectral evolution; (c) temporal profiles of the amplitude $|\rho_{AB}(0,\tau)|$ (solid blue) and phase $\phi(0,\tau)/\pi$ (solid black) at the point of maximum compression $\xi = 0$; (d) longitudinal profiles of phase $\phi(\xi,0)/\pi$ (solid black) and amplitude $\rho_{AB}(\xi,0)$ (solid blue), and overall wavenumber k_{1nl} (solid orange). Here $\beta_1 = -1$, $\delta k = 5$, $\Omega = 0.3$.

The phase-matching is ruled by Eqs. (14) already developed for the two-soliton case, where k_{loc} is a local contribution to the nonlinear wavenumber, which, for the AB, reads explicitly as

$$k_{\mathrm{loc}}(\xi,0) = \left.\frac{\partial \phi_{\mathrm{loc}}}{\partial \xi}\right|_{(\xi,0)} = \frac{\kappa b^2(\sqrt{2a}\cosh(\xi_n) + 1 - 4a)}{b^2 \sinh(\xi_n) + [(1-4a)\cosh(\xi_n) + \sqrt{2a}]^2}. \tag{17}$$

Here $\phi_{\mathrm{loc}}(\xi,0)$ is the longitudinal phase profile of the AB envelope extracted from Eq. (16):

$$\phi_{\mathrm{loc}}(\xi,0) = \tan^{-1}\left[\frac{b \sinh \xi_n}{(1-4a)\cosh(\xi_n) + \sqrt{2a}}\right]. \tag{18}$$

As a result, the overall wavenumber $\kappa + k_{\mathrm{loc}}$ reported by the orange solid line in Fig. 10(d), shows a bump around the maximum compression point, where the phase exhibits a steep variation.

In order to assess the role of the RR for the AB in quadratic media, we have numerically integrated Eqs. (1), starting from a weakly modulated background which corresponds to the AB solution (16), i.e., $u_1(\xi_0,\tau) = \rho_{AB}(\xi_0,\tau)$ and $u_2(\xi_0,\tau) = \rho_{AB}^2(\xi_0,\tau)\exp(i\delta k\xi_0)/\delta k$, with $\xi_0 = -20$. We report in Fig. 11 the features of the propagating quadratic AB. As shown in Figs. 11(a) and 11(b), the quadratic AB still exhibits the characteristic growth and decay cycle,

though the focus point is spatially delayed (i.e., the compression point is shifted forward from $\xi = 0$) due to the relatively small value of mismatch $\delta k = 5$, which causes a small deviation from the exact solution compared with the NLS equation. More importantly, the SH component clearly exhibits a new feature, namely the emission of RR at the compression point. This is also evident from the spectral evolutions shown in Figs. 11(c) and 11(d). The strong spectral broadening associated with the temporal compression seeds the RR emitted at frequency detuning $\omega_{2RR}^{\pm} = \pm 3.29$ around the SH, as shown in Fig. 11(d). Such frequencies are then down-converted to generate the weaker RR around the FF with detuning $\omega_{1FC}^{\pm} = \omega_{2RR}^{\pm}$, as displayed in Fig. 11(c). The RR frequencies remain constant during the evolution, and agree well with the predictions from Eq. (14b), as shown by the dashed lines in Figs. 11(c) and 11(d) and by the bullets in the output spectral cuts indicated in the top panels.
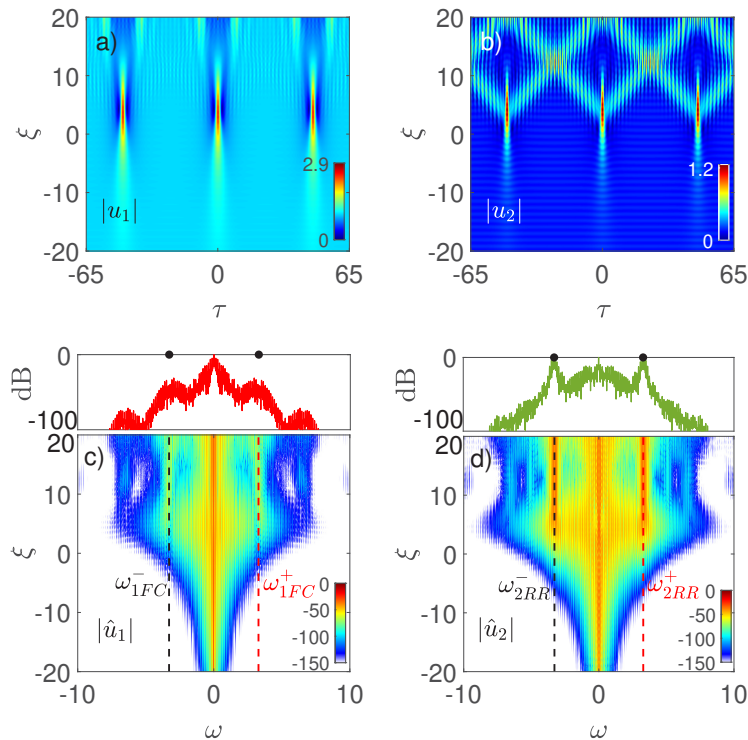

Fig. 11. Spatiotemporal envelope dynamics of the (a) FF and (b) SH components and their corresponding spectra (c) and (d). The top panels in (c) and (d) show the spectral profiles of FF and SH waves at output $\xi = 20$, wherein the bullets indicate the RR frequencies predicted through Eq. (14b). Here $\beta_1 = -1$, $\beta_2 = 1$, $\delta k = 5$, and $\Omega = 0.3$ ($a = 0.488$, $b = 0.296$).

Noteworthily, in Fig. 11(b), the RRs at the two opposite detunings travel in opposite directions. Therefore, due to the temporal periodic nature of the AB, the RR shed from the adjacent peaks undergoes coherent superposition that locally enhances the intensity of the RR at the crossing points. We point out, however, that the RR around both the FF and the SH does not exchange energy after the elastic collisions, as shown in Fig. 12, which corresponds to the temporal evolution of the frequency components filtered around $\omega_{1FC}^{+} = \omega_{2RR}^{+} = +3.29$ (a similar result holds when filtering around the image frequencies $\omega_{1FC}^{-} = \omega_{2RR}^{-} = -3.29$).

The RR clearly appears as shoulders in the discrete (i.e., comb-like) spectrum at any distance beyond the AB focus point. Figure 13 compares the spectra at FF and SH for two different distances $\xi = 5$ and $\xi = 10$. The spectra exhibit the comb structure with characteristic separation
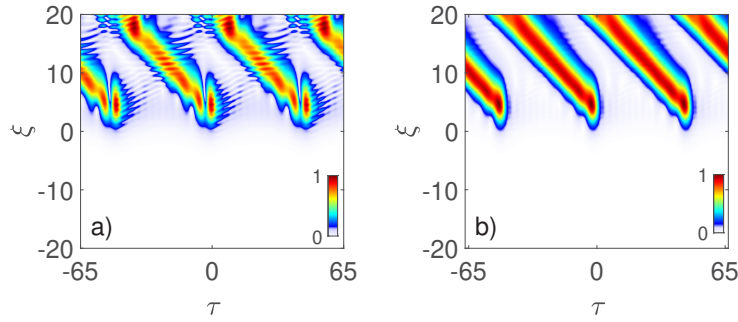
Fig. 12. Spatiotemporal evolution at (a) FF and (b) SH corresponding to Fig. 11, after filtering around the predicted RR frequency $\omega_{1FC}^+ = \omega_{2RR}^+ = +3.29$.

$\omega_p = \Omega\sqrt{\kappa}$ fixed by the modulation frequency Ω and the SHG mismatch parameter (see insets therein), and are fully overlapped at the two chosen distances $\xi = 5, 10$.
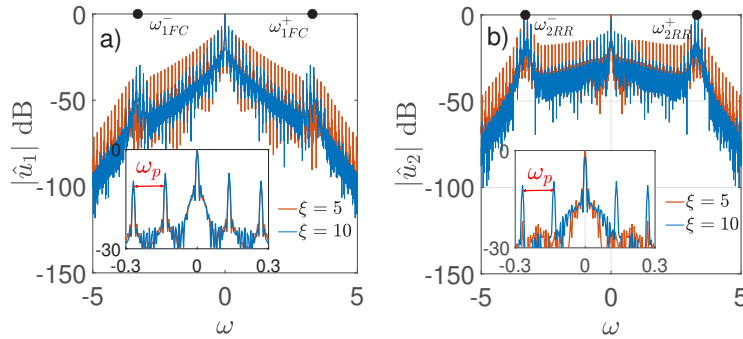

Fig. 13. Spectral profiles of the (a) FF and (b) SH components at $\xi = 5$ and $\xi = 10$, under the same parameters as in Fig. 11. The insets show zoomed pictures around central frequencies and the parameter $\omega_p = \Omega\sqrt{\kappa}$ defines the spacing of comb lines.

Finally, we summarize in Fig. 14 the dependence of the RR frequency on the SHG mismatch δk and GVD ratio β_2, which are obtained from multiple numerical simulations. As shown, also in this case, the simple phase-matching argument that leads to the theoretical predictions in Eq. (14b) still agrees well with the data extracted from numerical simulations.
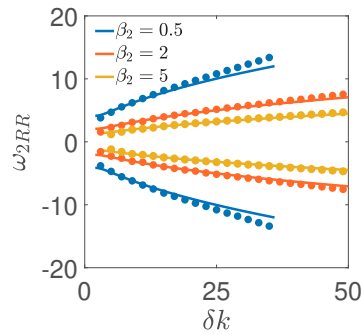

Fig. 14. Resonant frequencies $\omega_{2RR} = \omega_{2RR}^\pm$ versus normalized mismatch δk at different β_2, with theoretical prediction from Eq. (14b) (solid lines) compared with numerical simulations (dots). Here $\beta_1 = -1, \Omega = 0.3$.

6. Fundamental dark solitons

The RR mechanism investigated here is also valid for dark solitons supported by cascaded SHG. Here, we consider the example of a black stationary soliton, with an invariant envelope at FF,

$$\rho_{\text{dark}}(\xi, \tau) = \tanh(\sqrt{\kappa}\tau)\exp(i\kappa\xi), \qquad (19)$$

which exists, assuming again $\delta k > 0$, for $\beta_1 = 1$ (normal GVD), with nonlinear shift $\kappa = 1/\delta k$. The emission of RR around the SH component $u_2(\xi, \tau) = [\rho_{\text{dark}}^2(\xi, \tau)/\delta k]\exp(i\delta k\xi)$ is still governed by Eq. (9b), which now requires $\beta_2 > 0$, i.e., the same GVD sign at FF and SH (opposite to the condition $\beta_1\beta_2 < 0$ for bright solitons). As shown in Fig. 15, as an example for $\beta_2 = 3$ and $\delta k = 5$, the RR primary peaks at $\omega_{2RR}^{\pm} \simeq \pm 1.9$ and the down-converted peaks around the FF at $\omega_{1FC}^{\pm} = \omega_{2RR}^{\pm}$, are still accurately captured by the estimate from Eq. (9b), reported as vertical dashed lines in Figs. 15(c) and 15(d). Noteworthily, the RR is also evident in the temporal domain, especially at SH [see Fig. 15(b)], and now manifests itself as a spatiotemporal pattern formed by the interference of the longitudinal oscillation of the plane-wave background caused by periodic SHG conversion and back-conversion, while the radiation still travels away from the soliton central core. Similar to the case of bright solitons discussed in Fig. 4, the strength (or efficiency) of the RR is found (data not shown) to decrease with the larger mismatches (which would yield weaker nonlinearities) and the smaller β_2 (which results in too large RR frequencies to be efficiently seeded). Moreover, the higher-order dark solitons generated from input $\rho_{\text{dark}}(0, \tau) = N\tanh(\sqrt{\kappa}\tau)$, with N integer, radiate less efficiently than their bright counterparts, since they exhibit temporal
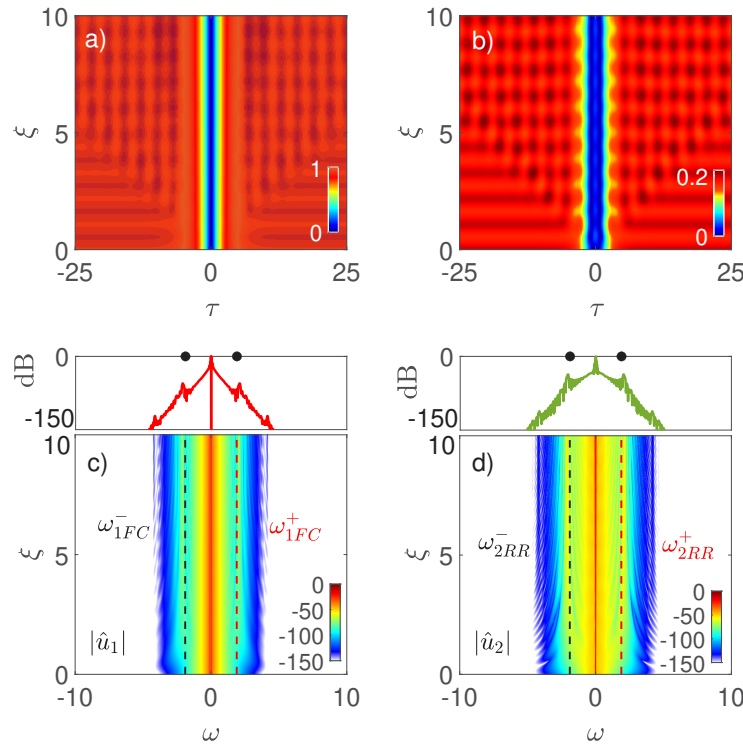

Fig. 15. Radiating black soliton: numerical spatiotemporal dynamics of (a) FF and (b) SH, and their corresponding spectra (c) and (d) with output profiles in the upper insets. Dashed lines in (c) and (d) as well as bullets in the upper insets stand for $\omega_{2RR}^{\pm} = \omega_{1FC}^{\pm}$ calculated from Eq. (9b). Here $\beta_1 = 1$, $\beta_2 = 3$, and $\delta k = 5$.

splitting [52] rather than the periodic compression and spectral broadening discussed in Sec. 4. Finally we point out that, for dark solitons, though, in principle, primary RR around the FF can arise also from Eq. (9a), the resulting frequencies are too small (embedded in the core spectrum of the soliton) to show any appreciable growth.

7. Conclusions

In summary, we have investigated the generation of optical RR in the cascading SHG process, through numerical simulation of the full coupled propagation equations. Our results considerably extend the understanding of the RR radiated by different quadratic solitary waves, including but not limited to the fundamental solitons, the second-order solitons, the ABs, and the dark solitons. What emerges is a common mechanism where RR is shed around the less intense SH component and then down-converted to take place around the FF via frequency mixing processes. The radiated frequency can be predicted by means of a simple universal phase-matching formula which we have validated in a wide region of the material parameters. These studies provide a novel perspective on solitary wave propagation in quadratic media and may pave the wave for generating new controllable frequency combs of interest in experiments.

Disclosures. The authors declare no conflicts of interest.

Data availability. Data underlying the results presented in this paper are not publicly available at this time but may be obtained from the authors upon reasonable request.

References

1. N. Akhmediev and M. Karlsson, "Cherenkov radiation emitted by solitons in optical fibers," Phys. Rev. A **51**(3), 2602–2607 (1995).
2. P. K. A. Wai, C. R. Menyuk, Y. C. Lee, and H. H. Chen, "Nonlinear pulse propagation in the neighborhood of the zero-dispersion wavelength of monomode optical fibers," Opt. Lett. **11**(7), 464–466 (1986).
3. A. S. Gouveia-Neto, M. E. Faldon, and J. R. Taylor, "Solitons in the region of the minimum group-velocity dispersion of single-mode optical fibers," Opt. Lett. **13**(9), 770–772 (1988).
4. J. P. Gordon, "Dispersive perturbations of solitons of the nonlinear Schrödinger equation," J. Opt. Soc. Am. B **9**(1), 91–97 (1992).
5. V. I. Karpman, "Radiation by solitons due to higher-order dispersion," Phys. Rev. E **47**(3), 2073–2082 (1993).
6. M.-C. Chan, C.-H. Lien, J.-Y. Lu, and B.-H. Lyu, "High power NIR fiber-optic femtosecond Cherenkov radiation and its application on nonlinear light microscopy," Opt. Express **22**(8), 9498–9507 (2014).
7. M.-T. Tsai and M.-C. Chan, "Simultaneous 0.8, 1.0, and 1.3 μm multispectral and common-path broadband source for optical coherence tomography," Opt. Lett. **39**(4), 865–868 (2014).
8. X. M. Liu, A. S. Svane, J. Laegsgaard, H. Tu, S. A. Boppart, and D. Turchinovich, "Progress in Cherenkov femtosecond fiber lasers," J. Phys. D: Appl. Phys. **49**(2), 023001 (2016).
9. I. Cristiani, R. Tediosi, L. Tartara, and V. Degiorgio, "Dispersive wave generation by solitons in microstructured optical fibers," Opt. Express **12**(1), 124–135 (2004).
10. L. Yin, Q. Lin, and G. P. Agrawal, "Soliton fission and supercontinuum generation in silicon waveguides," Opt. Lett. **32**(4), 391–393 (2007).
11. D. V. Skryabin and A. V. Gorbach, "Colloquium: Looking at a soliton through the prism of optical supercontinuum," Rev. Mod. Phys. **82**(2), 1287–1299 (2010).
12. C. Milián, A. Ferrando, and D. V. Skryabin, "Polychromatic Cherenkov radiation and supercontinuum in tapered optical fibers," J. Opt. Soc. Am. B **29**(4), 589–593 (2012).
13. R. Sollapur, D. Kartashov, M. Zürch, A. Hoffmann, T. Grigorova, G. Sauer, A. Hartung, A. Schwuchow, J. Bierlich, J. Kobelke, M. Chemnitz, M. A. Schmidt, and C. Spielmann, "Resonance-enhanced multi-octave supercontinuum generation in antiresonant hollow-core fibers," Light: Sci. Appl. **6**(12), e17124 (2017).
14. Y. Okawachi, M. Yu, J. Cardenas, X. Ji, M. Lipson, and A. L. Gaeta, "Coherent, directional supercontinuum generation," Opt. Lett. **42**(21), 4466–4469 (2017).
15. V. Brasch, M. Geiselmann, T. Herr, G. Lihachev, M. H. P. Pfeiffer, M. L. Gorodetsky, and T. J. Kippenberg, "Photonic chip-based optical frequency comb using soliton Cherenkov radiation," Science **351**(6271), 357–360 (2016).
16. A. B. Matsko, W. Liang, A. A. Savchenkov, D. Eliyahu, and L. Maleki, "Optical Cherenkov radiation in overmoded microresonators," Opt. Lett. **41**(13), 2907–2910 (2016).
17. X. Guo, C.-L. Zou, H. Jung, Z. Gong, A. Bruch, L. Jiang, and H. X. Tang, "Efficient generation of a near-visible frequency comb via Cherenkov-like radiation from a Kerr microcomb," Phys. Rev. Appl. **10**(1), 014012 (2018).

18. M. Erkintalo, Y. Q. Xu, S. G. Murdoch, J. M. Dudley, and G. Genty, "Cascaded phase matching and nonlinear symmetry breaking in fiber frequency combs," Phys. Rev. Lett. **109**(22), 223904 (2012).

19. M. Conforti and S. Trillo, "Radiative effects driven by shock waves in cavity-less four-wave mixing combs," Opt. Lett. **39**(19), 5760–5763 (2014).

20. N. Y. Joly, J. Nold, W. Chang, P. Hölzer, A. Nazarkin, G. K. L. Wong, F. Biancalana, and P. S. J. Russell, "Bright spatially coherent wavelength-tunable deep-UV laser source using an Ar-filled photonic crystal fiber," Phys. Rev. Lett. **106**(20), 203901 (2011).

21. A. V. Buryak, P. D. Trapani, D. V. Skryabin, and S. Trillo, "Optical solitons due to quadratic nonlinearities: from basic physics to futuristic applications," Phys. Rep. **370**(2), 63–235 (2002).

22. P. Di Trapani, D. Caironi, G. Valiulis, A. Dubietis, R. Danielius, and A. Piskarskas, "Observation of temporal solitons in second-harmonic generation with tilted pulses," Phys. Rev. Lett. **81**(3), 570–573 (1998).

23. X. Liu, L. Qian, and F. Wise, "High-energy pulse compression by use of negative phase shifts produced by the cascade $\chi^{(2)}$:$\chi^{(2)}$ nonlinearity," Opt. Lett. **24**(23), 1777–1779 (1999).

24. S. Ashihara, J. Nishina, T. Shimura, and K. Kuroda, "Soliton compression of femtosecond pulses in quadratic media," J. Opt. Soc. Am. B **19**(10), 2505–2510 (2002).

25. M. Marangoni, C. Manzoni, R. Ramponi, G. Cerullo, F. Baronio, C. D. Angelis, and K. Kitamura, "Group-velocity control by quadratic nonlinear interactions," Opt. Lett. **31**(4), 534–536 (2006).

26. M. Bache, O. Bang, J. Moses, and F. W. Wise, "Nonlocal explanation of stationary and nonstationary regimes in cascaded soliton pulse compression," Opt. Lett. **32**(17), 2490–2492 (2007).

27. M. Bache, O. Bang, B. B. Zhou, J. Moses, and F. W. Wise, "Optical Cherenkov radiation in ultrafast cascaded second-harmonic generation," Phys. Rev. A **82**(6), 063806 (2010).

28. B. B. Zhou, A. Chong, F. W. Wise, and M. Bache, "Ultrafast and octave-spanning optical nonlinearities from strongly phase-mismatched quadratic interactions," Phys. Rev. Lett. **109**(4), 043902 (2012).

29. M. Conforti, N. Westerberg, F. Baronio, S. Trillo, and D. Faccio, "Negative-frequency dispersive wave generation in quadratic media," Phys. Rev. A **88**(1), 013829 (2013).

30. B. Zhou, H. Guo, and M. Bache, "Soliton-induced nonlocal resonances observed through high-intensity tunable spectrally compressed second-harmonic peaks," Phys. Rev. A **90**(1), 013823 (2014).

31. B. Zhou, H. Guo, and M. Bache, "Energetic mid-IR femtosecond pulse generation by self-defocusing soliton-induced dispersive waves in a bulk quadratic nonlinear crystal," Opt. Express **23**(5), 6924–6936 (2015).

32. B. Zhou and M. Bache, "Dispersive waves induced by self-defocusing temporal solitons in a beta-barium-borate crystal," Opt. Lett. **40**(18), 4257–4260 (2015).

33. B. Zhou, X. Liu, H. Guo, X. Zeng, X. Chen, H. ping Chung, Y.-H. Chen, and M. Bache, "Parametrically tunable soliton-induced resonant radiation by three-wave mixing," Phys. Rev. Lett. **118**(14), 143901 (2017).

34. L. Bu, F. Baronio, S. Chen, and S. Trillo, "Quadratic Peregrine solitons resonantly radiating without higher-order dispersion," Opt. Lett. **47**(10), 2370–2373 (2022).

35. F. Baronio, S. Chen, and S. Trillo, "Resonant radiation from Peregrine solitons," Opt. Lett. **45**(2), 427–430 (2020).

36. N. Akhmediev and V. Korneev, "Modulation instability and periodic solutions of the nonlinear Schrödinger equation," Theor. Math. Phys. **69**(2), 1089–1093 (1986).

37. F. Baronio, "Akhmediev breathers and Peregrine solitary waves in a quadratic medium," Opt. Lett. **42**(9), 1756–1759 (2017).

38. R. Schiek and F. Baronio, "Spatial Akhmediev breathers and modulation instability growth-decay cycles in a quadratic optical medium," Phys. Rev. Res. **1**(3), 032036 (2019).

39. R. Schiek, "Excitation of nonlinear beams: from the linear Talbot effect through modulation instability to Akhmediev breathers," Opt. Express **29**(10), 15830–15851 (2021).

40. A. G. Kalocsai and J. W. Haus, "Nonlinear Schrödinger equation for optical media with quadratic nonlinearity," Phys. Rev. A **49**(1), 574–585 (1994).

41. C. R. Menyuk, R. Schiek, and L. Torner, "Solitary waves due to $\chi^{(2)}$:$\chi^{(2)}$ cascading," J. Opt. Soc. Am. B **11**(12), 2434–2443 (1994).

42. J. Moses and F. W. Wise, "Soliton compression in quadratic media: high-energy few-cycle pulses with a frequency-doubling crystal," Opt. Lett. **31**(12), 1881–1883 (2006).

43. J. Moses, B. A. Malomed, and F. W. Wise, "Self-steepening of ultrashort optical pulses without self-phase-modulation," Phys. Rev. A **76**(2), 021802 (2007).

44. M. Conforti, F. Baronio, and S. Trillo, "Dispersive shock waves in phase-mismatched second-harmonic generation," Opt. Lett. **37**(6), 1082–1084 (2012).

45. F. Baronio, S. Chen, and D. Mihalache, "Two-color walking Peregrine solitary waves," Opt. Lett. **42**(18), 3514–3517 (2017).

46. J. Satsuma and N. Yajima, "Initial value problems of one-dimensional self-modulation of nonlinear waves in dispersive media," Prog. Theor. Phys. Suppl. **55**, 284–306 (1974).

47. M. Fejer, G. Magel, D. Jundt, and R. Byer, "Quasi-phase-matched second harmonic generation: tuning and tolerances," IEEE J. Quantum Electron. **28**(11), 2631–2654 (1992).

48. A. Mussot, M. Conforti, S. Trillo, F. Copie, and A. Kudlinski, "Modulation instability in dispersion oscillating fibers," Adv. Opt. Photonics **10**(1), 1–42 (2018).

49. M. Conforti, S. Trillo, A. Mussot, and A. Kudlinski, "Parametric excitation of multiple resonant radiations from localized wavepackets," Sci. Rep. **5**(1), 9433 (2015).
50. R. Driben, A. V. Yulin, and A. Efimov, "Resonant radiation from oscillating higher order solitons," Opt. Express **23**(15), 19112–19117 (2015).
51. K. Hammani, B. Kibler, C. Finot, P. Morin, J. Fatome, J. M. Dudley, and G. Millot, "Peregrine soliton generation and breakup in standard telecommunications fiber," Opt. Lett. **36**(2), 112–114 (2011).
52. A. Fratalocchi, C. Conti, G. Ruocco, and S. Trillo, "Free-energy transition in a gas of noninteracting nonlinear wave particles," Phys. Rev. Lett. **101**(4), 044101 (2008).